Exploring electron density distributions for the complete valence shell of cyclopentene using a binary $(e,2e)$ spectrometer

X. G. Ren, C. G. Ning, S. F. Zhang, G. L. Su, B. Li, H. Zhou, F. Huang, G. Q. Li, and J. K. Deng*
Department of Physics and Key Laboratory of Atomic and Molecular NanoSciences of MOE, Tsinghua University, Beijing 100084, People's Republic of China
(Received 11 November 2004; revised manuscript received 27 May 2005; published 16 November 2005)

The measurements of electron density distributions and binding-energy spectrum of the complete valence shell of cyclopentene (C_5H_8) using a binary $(e,2e)$ electron momentum spectrometer are reported. The experimental momentum profiles of the valence orbitals are compared with the theoretical distributions calculated using Hartree-Fock and density-functional-theory (DFT) methods with various basis sets. The agreement between theory and experiment for the shape and intensity of the orbital electron momentum distributions is generally good. The DFT calculations employing B3LYP hybrid functional with a saturated and diffuse AUG-CC-PVTZ basis set provide the better descriptions of the experimental data. Some "turn up" effects in the low momentum region of the measured $(e,2e)$ cross section compared with the calculations of $3a''$, $2a''$, and $3a'$ orbitals could be mainly attributed to distorted-wave effects. The pole strengths of the main ionization peaks from the orbitals in the inner valence are estimated.

DOI: 10.1103/PhysRevA.72.052712 PACS number(s): 34.80.Gs, 31.15.Ar

I. INTRODUCTION

Recently, cyclic unsaturated hydrocarbons such as cyclopentene (C_5H_8) have been widely used for the fabrication of ordered organic monolayer films on the group IV semiconductor surfaces of crystalline silicon (Si) [1–7], germanium (Ge) [8], and diamond (C) [9], and form the organic-semiconductor hybrid materials, which provide a favorable linking of organic chemistry to existing semiconductor-based microelectronic technologies and open technological opportunities in semiconductor-based microelectronic devices because of the possibility of combining the wide range of functionality of organic molecules with the semiconductor substrate. Therefore, the interaction of organic molecules with a semiconductor surface represents an area of significant scientific and technological interest because of its importance in surface chemistry. According to some experimental [2–8] and theoretical [1,9] studies, such a surface chemistry reaction between cyclic unsaturated hydrocarbons and the semiconductor surface was explained by the so-called [2+2] cycloaddition mechanism where the interaction between such cyclic hydrocarbons and the Si, Ge, and C (diamond) surface is facilitated by the interaction of the C=C π bond of unsaturated hydrocarbons with the Si=Si, Ge=Ge, and C=C (diamond) dangling bonds of a semiconductor dimmer to form two strong new X—C σ bonds (X=Si, Ge, and C). In the reaction chemistry, such useful properties as molecule structure, chemical bonding, binding energies, momentum profiles, and orbital electron density distributions of the valence orbitals in the reactant molecules such as cyclic unsaturated cyclopentene are particularly important for chemical reactivity and possibly molecular recognition [10,11]. Therefore, the investigations for these useful properties of the valence orbitals by the binary $(e,2e)$ coincidence experiment and the associate theoretical calculations are essential due to some significant information they provide for understanding the chemical adsorption or cycloaddition reaction between cyclopentene and the semiconductor surface.

Another motivation of the present work is that the conformation of the cyclic unsaturated cyclopentene is of interest to many structural chemists, who have applied a wide variety of experimental and theoretical methods in their investigations [12,13]. The cycloalkenes are of particular interest because of the analogies that can be drawn between their conformations and those of the saturated rings containing one fewer carbon atom.

Electron momentum spectroscopy (EMS), also known as binary $(e,2e)$ spectroscopy, is a kinematically complete ionization process [14–16]. The unique measurement for the electron momentum distributions of an individual molecular orbital has made it become a powerful tool for experimental electronic structure studies of atoms, molecules, and solids [16]. In the $(e,2e)$ ionization reaction, the differences between the observed final and initial total electron energies and momenta are, respectively, the energy eigenvalue of the corresponding state of the residual ion and the momentum of the struck electron at the collision instant. From an ensemble of ionization events, binding-energy spectra are obtained over a wide energy range by keeping the energies of the two emitted electrons fixed and varying the incident energy. And electron momentum distributions for an individual orbital in the molecule can be obtained by measuring the EMS cross section, at a fixed value of the binding energy, as a function of the azimuthal angle ϕ between the two emitted electrons. The momentum distribution information provides powerful proof for evaluating the quality of quantum chemical calculations [14–16] at the Hartree-Fock (HF) level and also of correlated treatments such as configuration-interaction (CI) methods and density-functional theory (DFT). EMS mea-

*Corresponding author. Electronic address: djkdmp@mail.tsinghua.edu.cn

 ©2005 The American Physical Society

surements and high-level quantum-mechanical calculations can provide a sensitive probe of the binding energies, orbital electron density distributions, molecular structure and conformation, chemical bonding, and reactivity in the chemical important outer spatial regions of atoms and molecules. Furthermore, since electron momentum distribution is sensitive to diffuse parts of the position wave function, EMS can provide information relevant to issues of chemical reaction and molecular recognition, and the momentum space electron density may be a criterion for molecular similarity and dissimilarity [17].

In the present work, the electron density distributions for the complete valence shell of cyclopentene (C_5H_8) and binding-energy spectra (2–34 eV) were measured at an impact energy of 1200 eV plus binding energy using an energy-dispersive multichannel $(e,2e)$ electron momentum spectrometer employing symmetric noncoplanar geometry. The experimental momentum profiles are compared with the theoretical momentum distributions calculated using HF and DFT methods with the various basis sets ranging from STO-3G to AUG-CC-PVTZ in quality.

II. THEORETICAL BACKGROUND OF EMS

In a typical EMS experiment, the relative $(e,2e)$ cross section for an electron impact ionization experiment is measured by detecting the two outgoing electrons in coincidence, angularly selected and energy-analyzed by lens systems and electrostatic analyzers. The particular kinematics of the experiment is chosen in such a way as to provide a straightforward relation between some variable kinematic parameters and the momentum of the ionized electron prior to knockout. The symmetric noncoplanar kinematics [14–16] is the frequently used experimental configuration.

In the symmetric noncoplanar scattering geometry, the two outgoing electrons are selected to have equal polar angles ($\theta_1=\theta_2=45°$) relative to the incident electron beam. The azimuthal (out-of-plane) angle ϕ between the two outgoing electrons is variable over the range of 0° to ±30° around the incident beam axis. Under these high impact energy and large momentum transfer conditions, the plane-wave impulse approximation (PWIA) provides a good description of the collision [16] and the ionized electron essentially undergoes a clean "knock-out" collision [10]. The momentum p of the ejected electron prior to knockout is related to the azimuthal angle by [14–16]

$$p=\{(2p_1\cos\theta_1-p_0)^2+[2p_1\sin\theta_1\sin(\phi/2)]^2\}^{1/2}, \quad (1)$$

where p_1 and p_0 are the momenta of the outgoing and incident electrons, respectively. If the incident electron energy is varied, a binding-energy spectrum (BES) can be recorded at each azimuthal angle ϕ. Variation of ϕ at a given binding energy therefore yields an orbital electron momentum (density) distribution. The EMS reaction theory is based on several approximations [14–16,18], including the binary encounter approximation (in which the residual ion is a mere spectator and hence the collision operator depends only on the incident and recoil electrons), and the PWIA, through which the binary $(e,2e)$ cross section (σ_{EMS}) for the randomly oriented molecules is proportional to the spherically averaged momentum distribution of the corresponding Dyson orbital [10,14]. The expression for σ_{EMS} can be given by

$$\sigma_{\mathrm{EMS}}\propto\int d\Omega|\langle p\Psi_f^{N-1}|\Psi_i^N\rangle|^2, \quad (2)$$

where p is the momentum of the target electron prior to ionization. $|\Psi_f^{N-1}\rangle$ and $|\Psi_i^N\rangle$ are the total electronic wave functions for the $N-1$ electron final (ion) state and the N-electron target molecule ground (initial) state, respectively. The $\int d\Omega$ represents an integral over all angles (spherical averaging) due to averaging over all initial rotational states for the randomly oriented gas phase target. The average over the initial vibrational states is well approximated by evaluating orbitals at the equilibrium geometry of the molecule. Final rotational and vibrational states are eliminated by closure [10,14,16]. The overlap of the ion and neutral wave functions in Eq. (2) is known as a Dyson orbital.

By using the target Hartree-Fock approximation (THFA) [16] or the target Kohn-Sham approximation (TKSA) [18,19], in which the Dyson orbital is approximated with the neutral state canonical HF or Kohn-Sham (KS) orbital, the EMS cross section can be further simplified by

$$\sigma_{\mathrm{EMS}}\propto S_j^{(f)}\int d\Omega|\psi_j(p)|^2, \quad (3)$$

where $|\psi_j(p)\rangle$ is the one-electron momentum space canonical HF or KS orbital wave function in the neutral initial state for the jth electron that was ionized. The spectroscopic factor $S_j^{(f)}$ is the square of the spectroscopic amplitude for orbital j and ion state f. The integral in Eq. (3) is known as the spherically averaged one-electron momentum distribution (MD). Therefore, EMS has the ability to image the electron density distribution in an individual orbital selected according to their binding energies.

TKSA includes an accounting for initial-state electron correlation effects via the DFT exchange correlation potential [10,19]. The THFA and TKSA treatments constitute two different levels of the orbital approximation and thus they provide a direct means of evaluating the $(e,2e)$ cross section in terms of the electron momentum density distribution. The HF and KS momentum space wave functions in Eqs. (2) and (3), respectively, may be converted into their more familiar position space counterparts, and thus also into the corresponding position space orbital electron densities by Fourier transformation.

III. EXPERIMENTS AND CALCULATIONS

The experiment was carried out using an energy-dispersive multichannel electron momentum spectrometer, for which the details of construction and operation at Tsinghua University have been reported earlier [20]. Briefly, in our EMS experiment, the target molecules are ionized by a beam of electrons with impact electron energy of 1200 eV plus the binding energy. Two outgoing electrons are sampled over a range of energies ($E_1=596-604$ eV, $E_2=596-604$ eV) by hemispherical analyzers and detected in coincidence using

time-correlated position-sensitive microchannel plate detectors in the energy-dispersive exit planes of the analyzers. One analyzer can be rotated around the beam axis over a range of relative azimuthal angles ϕ, from 0° to ±30°. The electron coincidence counts are recorded at each ϕ value as the impact energy is varied and this procedure results in a series of angularly resolved BES. The momentum of the target electron, immediately prior to impact, is observed within a very close approximation. The experimental momentum profile (XMP), i.e., the spherically averaged momentum distribution, is obtained by recording the coincidence counts while varying the relative azimuthal angle at a given binding energy. By using Eq. (1), the azimuthal angle ϕ can be related to the momentum p of the ionized electron [14].

The theoretical momentum profiles (TMPs) were calculated within the THFA or TKSA using the HEMS program developed at UBC. This procedure calculates a Fourier transform of a given position space molecular orbital and then performs spherical averaging of its square (orbital momentum density). The position space molecular orbitals were calculated using the GAUSSIAN 98 program. The molecular geometry of cyclopentene was obtained from the experimental and theoretical analysis by Boggs *et al.* [12,13] and further optimization was processed by using the DFT-B3LYP calculation with the AUG-CC-PVTZ basis set. The canonical HF orbitals for cyclopentene were calculated by using Eq. (3) with the STO-3G [21,22], 6-31G [23], 6-311++G^{**} [24,25] basis sets and the augmented correlation consistent polarized valence triple zeta basis set (AUG-CC-PVTZ), which was taken from the work of Dunning *et al.* [26,27]. The KSOs were found by running DFT calculations utilizing the B3LYP hybrid gradient corrected functional with these basis sets. It should be noted that the theoretical momentum profiles $\rho_{\mathrm{TMP}}(p)$ of each valence orbital are normalized such that

$$\int_0^\infty \rho_{\mathrm{TMP}}(p)p^2dp = \frac{1}{4\pi}. \tag{4}$$

In order to compare the calculated cross sections with the experimental momentum profiles, the effects of the finite spectrometer acceptance angles in both θ and ϕ ($\Delta\theta = \pm 0.6°$ and $\Delta\phi = \pm 1.2°$) and the instrumental energy resolution of 1.2 eV (FWHM) obtained by the measurement of the argon $3p$ state were included by using the Gaussian-weighted planar grid (GWPG) method [28].

Cyclopentene was purchased from Fluka scientific and used as received. At room temperature, the volatility of the cyclopentene sample is high enough to create a sufficient concentration of target molecules in the gas phase. The data were collected in many repetitive scans at 12 different relative azimuthal angles ϕ over the binding-energy range of 2–34 eV, which covers the complete valence shell ionization region. The experimental momentum profiles for an individual orbital or groups of orbitals were obtained from the binding-energy spectra as described in the following section.

IV. RESULTS AND DISCUSSIONS

Cyclopentene (C_5H_8) has C_s point-group symmetry according to molecular orbital theory [12,13]. Its ground-state electronic configuration can be written as

$$(\mathrm{Core})^{10} \quad \underbrace{(1a')^2\,(2a')^2\,(1a'')^2\,(3a')^2}_{\text{Inner Valence}} \quad \underbrace{(2a'')^2\,(4a')^2\,(5a')^2\,(3a'')^2\,(6a')^2\,(7a')^2\,(4a'')^2\,(8a')^2\,(5a'')^2\,(9a')^2}_{\text{Outer Valence}}$$

All the molecular orbitals (MOs) are either a'-type or a''-type. The assignment of occupation for these valence orbitals has been discussed in PES experiments [29–31]. The outer valence shell Green function (OVGF) calculation of ionization potentials (IPs) and pole strengths for outer valence orbitals of C_5H_8 has also been performed, as shown in Table I.

A. Binding-energy spectrum

In order to obtain the experimental momentum profiles corresponding to the main peaks in the outer and inner valence regions, 12 binding-energy spectra over the energy range of 2–34 eV were collected at the out-of-plane relative azimuth angles ϕ=0°, 1°, 2°, 3°, 4°, 6°, 8°, 10°, 12°, 14°, 17°, and 22° in a series of sequential repetitive scans. The experimental binding-energy spectrum of C_5H_8 for the sum of all ϕ angles is shown in Fig. 1. This binding-energy spectrum was fitted with a series of individual Gaussian peaks. The relative energy values were given by the ionization potentials determined by high-resolution PES [29–31]. The widths of Gaussian peaks were combinations of EMS instrumental energy resolution and Franck-Condon widths of the corresponding bands determined by high-resolution PES [29,30]. Small adjustments have been applied to compensate for the asymmetries of the shapes of the Franck-Condon profiles. In Fig. 1, Gaussian peaks fitted to the individual transitions are shown by dashed lines while their sum is represented by the solid line.

The outer valence shell ionization potentials have been reported by Bieri *et al.* in Ref. [29] using He I radiation source. In the PES work, the vertical ionization potential of the $9a'$ HOMO was 9.18 eV and the $5a''$, $8a'$, $4a''$, $7a'$, $6a'$, $3a''$, $5a'$, and $4a'$ orbitals were determined to be 11.6, 12.0, 12.2, 12.6, 13.1, (14.0), 15.8, and 16.1 eV, respectively. Other PES studies of cyclopentene were reported by Wiberg and Ellison *et al.* [30] using He I and He II radiation source, which included some of the inner valence region of C_5H_8, and the ionization potential of the $9a'$ HOMO was 9.20 eV. The $5a''$, $8a'$, $4a''$, $7a'$, $6a'$, $3a''$, $5a'$, $4a'$, and $2a''$ orbitals were determined to be 11.6, 12.0, 12.2, 12.6, 13.08, 14.0, 15.8, 16.1, and 17.3 eV, respectively. In the inner valence

TABLE I. Ionization energies (eV) and pole strength for C_5H_8.

	Experimental results				Theoretical calculations		
Orbital	PES[a]	PES[b]	PES[c]	EMS[d]	MO[a] character	Ionization[e] potential	Pole[c] strength
$9a'$	9.18	9.20		9.15	πC═C	9.122	0.913
$5a''$	11.6	11.6			σC—C$^-$	11.804	0.907
$8a'$	12.0	12.0			σC—C$^+$	12.271	0.910
$4a''$	12.2	12.2		11.95	σC—C$^+$	12.156	0.905
$7a'$	12.6	12.6			σCH2	12.093	0.903
$6a'$	13.1	13.08			σC—C	13.128	0.904
$3a''$	14.0	14.0		14.19	πCH2$^-$	13.892	0.905
$5a'$	15.8	15.8		16.05	πCH2$^+$	15.926	0.897
$4a'$	16.1	16.1			σC—C$^+$	16.588	0.872
$2a''$		17.3		18.30		17.777	0.861
$3a'$		19.0	18.75				
$1a''$		22.0	22.04	22.30			
$2a'$				(0.76)[f]			
$1a'$			26.0	25.85 (0.52)[f]			

[a]From Ref. [29].
[b]From Ref. [30].
[c]From Ref. [31].
[d]This work.
[e]OVGF with 6-311++G** in this work.
[f]Experimental estimated spectroscopic factors in this work.

region, the vertical ionization potential of the $3a'$ inner valence orbital was 19.0 eV. The average vertical ionization potential of the $1a''$ and $2a'$ orbitals was 22.0 eV. The ionization potential at 26.0 eV was assigned to the innermost valence $1a'$ orbital by Streets and Potts [31].

In our EMS work, seven structures can be identified in the binding-energy spectrum of Fig. 1. The vertical ionization potential of HOMO $9a'$ is determined to be 9.15 eV. The averaged vertical ionization potentials of the $(5a''+8a'+4a''+7a'+6a')$, $3a''$, and $(5a'+4a')$ are determined to be 11.95, 14.19, and 16.05 eV, respectively. The ionization potentials at 18.30, 22.30, and 25.85 eV were assigned to the inner valence $(2a''+3a')$, $(1a''+2a')$, and $1a'$ orbitals, re-

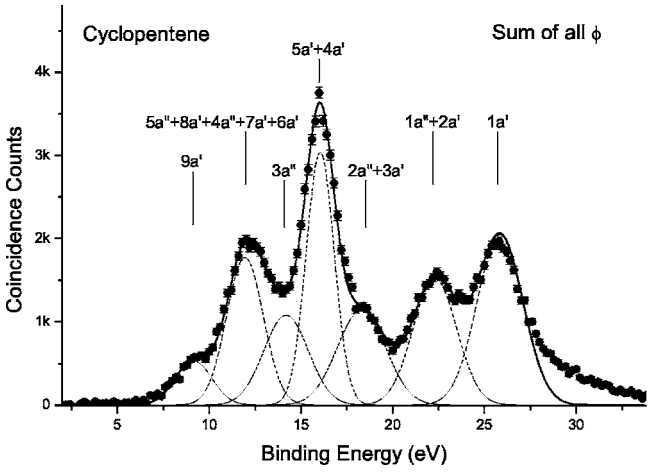

FIG. 1. The binding-energy spectrum of cyclopentene from 2 to 34 eV over all 12 ϕ angles. The dashed lines represent Gaussian fits to the peaks and the solid line is the summed fit. The vertical lines in the figure indicate the corresponding (mean) ionization potentials. See text for further details.

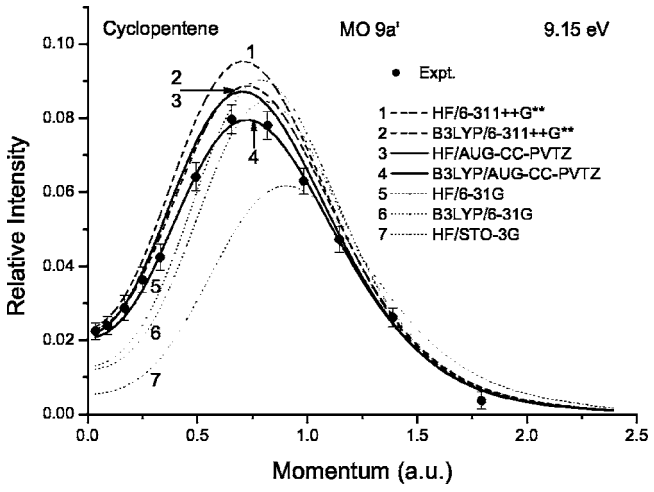

FIG. 2. Experimental and theoretical momentum distributions for the $9a'$ orbital of cyclopentene. The solid circles represent the experimental measurements derived from deconvolution procedures. The theoretical momentum profiles are calculated by using HF and DFT-B3LYP methods with various basis sets.

spectively. In addition, some rather weak satellite structures due to many-body correlation effects in the target or in the residual ion final states are also observed above 28.0 eV in the binding-energy spectrum. The differences in width are due to the vibrational broadening of the lines. The binding-energy values in Fig. 1 are consistent with the PES data [29–31].

The calculated ionization potentials obtained using Green's-function methods together with the measured PES, present EMS results, and molecular orbital character are shown in Table I. OVGF calculation also gives the pole strengths for the outer valence orbitals. As can be seen from Table I, the pole strengths for ionization from the outer valence orbitals (below the $3a''$ orbital in ionization energy) can be regarded as unity to some extent.

B. Momentum profiles

Deconvolving the binding-energy spectra measured at each of a chosen set of azimuthal angles by means of a least-squares-fit technique allows us to derive the momentum profiles associated with each of the bands identified in Fig. 1. The measured momentum profiles are not absolute, so the obtained relative magnitude needs to be normalized by an absolute scale [14,18]. Usually, this normalization factor is determined by normalizing the experimental and theoretical momentum distributions of the outermost valence ionization to the common intensity scale [10], since the outermost valence ionizations are expected to exhibit pole strength close to unity (in Table I). In this work, the HOMO $9a'$ orbital was used to determine this normalization factor. The experimental momentum profile of the $9a'$ orbital was placed on an absolute scale by normalizing this to the HF and DFT-B3LYP calculations with the 6-311++G^{**} and AUG-CC-PVTZ basis sets, respectively. And the best fit within these calculations to experimental data was obtained by normalizing the measured momentum profile of the $9a'$ orbital to the DFT-B3LYP method employing the AUG-CC-PVTZ basis set, and the normalization factor was also obtained from this normalization [18]. The same normalization factor is also preserved for the other experimental momentum profiles in Figs. 3–8.

The experimental and the theoretical momentum profiles for the $9a'$ orbital of cyclopentene are shown in Fig. 2. The experimental and theoretical momentum profiles show the expected "p-type" distribution (the experimental $p_{\max}$ $\sim$0.75 a.u.). Within the HF and DFT-B3LYP calculations with the 6-311++G^{**} and AUG-CC-PVTZ basis sets (curves 1–4), the B3LYP/AUG-CC-PVTZ calculation (curve 4) can provide a relatively good description for the experimental momentum profile of the $9a'$ orbital. The lower-level HF and DFT calculations with the 6-31G basis set (curves 5 and 6) underestimate the observed intensity in the low-momentum region and shift the position of the maximum a little to the high momentum end, while the HF calculation with the STO-3G minimal basis set (curve 7) produces a much lower intensity in the lower momentum region and shifts the maximum intensity position of $p_{\max}$.

The present $9a'$ orbital results indicate that for the HOMO orbital of cyclopentene, a calculated electron momentum density distribution of the corresponding KS orbitals gives a better description of the measured momentum profile. Since this diffuse larger r (lower p) region is particularly important for chemical reactivity and possibly molecular recognition [11,17], a proper quantitative quantum-mechanical description of such phenomena should include an adequate accounting for electron correlation. The DFT methods using the generalized gradient corrected functional B3LYP with saturated diffuse and Dunning's correlation, consistent basis sets [26,27] can provide a relatively good means of frontier behavior including electron correlation effects into quantum chemical calculations for chemical reactive cyclopentene in the adsorption or cycloaddition reaction between cyclopentene and semiconductor surface.

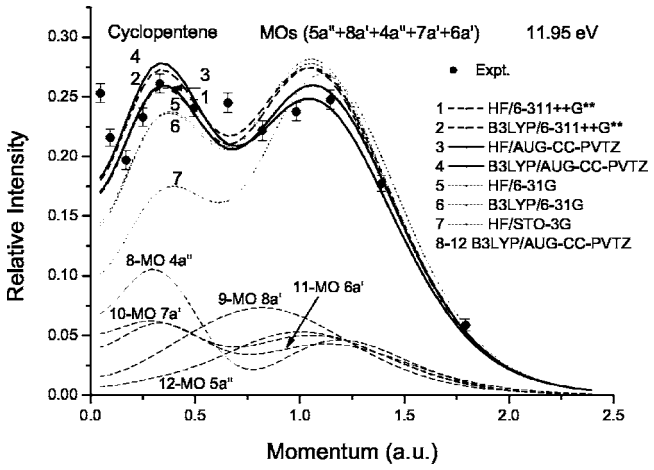

FIG. 3. Experimental ($5a''+8a'+4a''+7a'+6a'$) and theoretical momentum distributions for $5a''$, $8a'$, $4a''$, $7a'$, and $6a'$ and the sum of these individual orbitals of cyclopentene. The solid circles represent the experimental measurements derived from deconvolution procedures. The theoretical momentum profiles are calculated by using HF and DFT-B3LYP methods with various basis sets.

The second peak, positioned at 11.95 in the EMS binding-energy spectrum of Fig. 1, is due to the five outer valence orbitals ($5a''$, $8a'$, $4a''$, $7a'$, and $6a'$). The summed XMPs have a double-peak distribution peaked at $\sim$0.3 and $\sim$1.1 a.u., respectively, as shown in Fig. 3. The theoretical momentum profiles indicate that the $5a''$ and $8a'$ orbitals have a "p-type" distribution (curves 12 and 9) while the $4a''$, $7a'$, and $6a'$ orbitals have a double "p-type" distribution (curves 8, 10, and 11). The summed theoretical momentum distribution of these orbitals therefore has a double-peak distribution, consistent with the XMPs. The comparison of the summed XMPs with various calculations in Fig. 3 shows that the HF and DFT calculations with the AUG-CC-PVTZ basis set (curves 3 and 4) reproduce the experimental data reasonably well, particularly in the momentum region above 0.6 a.u., and these two calculations with the 6-311++G^{**} basis set (curves 1 and 2) overestimate experimental intensity in the above 0.6 a.u. momentum range. And the lower-level calculations with 6-31G and STO-3G basis sets (curves 5–7) underestimate the experimental intensity in the lower momentum region and overestimate the intensity in the high momentum region.

The experimental and theoretical momentum profiles for the $3a''$ orbital are shown in Fig. 4(a). The TMPs calculated

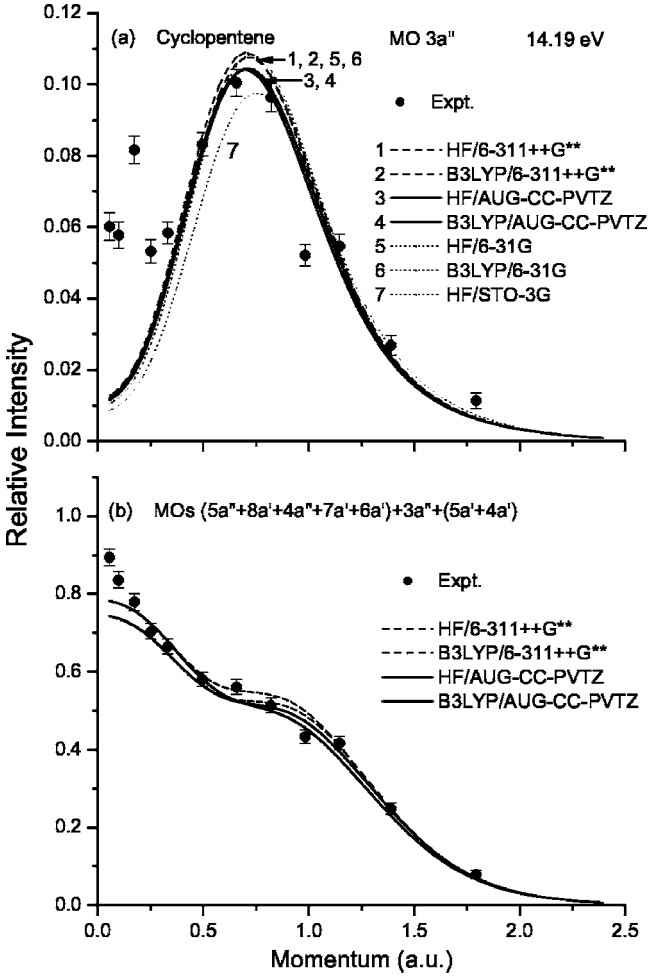

FIG. 4. Experimental and theoretical momentum distributions for (a) the $3a''$ orbital and (b) the summed $(5a''+8a'+4a''+7a'+6a')$, $3a''$, and $(5a'+4a')$ orbitals of cyclopentene. The solid circles represent the experimental measurements derived from deconvolution procedures. The theoretical momentum profiles are calculated by using HF and DFT-B3LYP methods with various basis sets.

by HF and DFT methods with various basis sets are very similar except for the HF calculation with the STO-3G minimal basis set. Somewhat better fits to the XMPs can be achieved using the HF and DFT-B3LYP methods with the AUG-CC-PVTZ basis set (curves 3 and 4) than the other level calculations with 6-311++G** and 6-31G basis sets (curves 1, 2, and 5–7). However, there is a significant discrepancy between the theoretical calculations and experimental data below the momentum of 0.3 a.u.; the TMPs underestimate the experimental intensity. The discrepancy between experiment and theory in the low momentum region is probably due to the "contamination" from the intensity of neighboring orbitals caused by the uncertainty in the curve-fitting procedures. In order to further investigate the explanation, the summed experimental data of the $(5a''+8a'+4a''+7a'+6a')$, $3a''$, and $(5a'+4a')$ orbitals are compared with the summed theoretical calculations as shown in Fig. 4(b). Again, the summed TMPs give a very reasonable description for the summed XMP above 0.3 a.u., and also underestimate the experimental data at the low momentum region. And the experimental momentum profiles adjacent to the $3a''$ orbital obtained with the same curve-fitting procedures can be well described by the corresponding TMPs. These indicate that the discrepancy between experimental data and the theoretical calculations below 0.3 a.u. for the $3a''$ orbital is not mainly due to a possible uncertainty in the curve-fitting procedures.

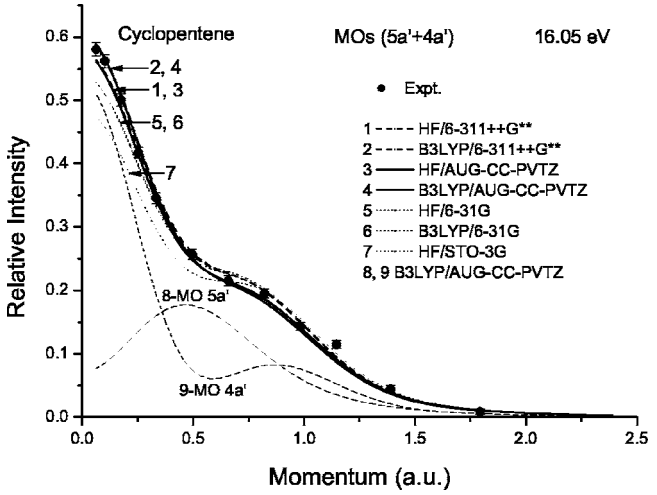

FIG. 5. Experimental $(5a'+4a')$ and theoretical momentum distributions for the $5a'$,$4a'$ orbitals and the sum of these individual orbitals of cyclopentene. The solid circles represent the experimental measurements derived from deconvolution procedures. The theoretical momentum profiles are calculated by using HF and DFT-B3LYP methods with various basis sets.

Another consideration for the discrepancy in the low momentum region could be due to the distorted wave effects since the $3a''$ orbital of cyclopentene is a π^*-like molecular orbital in symmetry [32–35]. Specifically atomic d orbitals and π^*-like molecular orbitals exhibit gerade-type symmetry and as a result zero gradient components of their position space wave functions in the nuclear (atoms) or internuclear (molecules) small r regions. Thus, low p components are expected at small r for such orbitals and therefore effects due to distortion of the incoming and outgoing electron waves may be reasonably expected to be manifested in the low p regions of such XMPs [32–34]. The further comparison between the experimental electron momentum profiles for Xe $4d$ orbitals and the theoretical calculations considering distorted wave effects strongly suggests that these "turn up" effects of $(e,2e)$ cross sections in the low-p region are due to the distorted wave effects [32,33]. Unfortunately at present, distorted wave calculations are possible only for atoms but not for molecules due to the multicenter nature for the molecule targets. Recently, the $(e,2e)$ experiments in ethylene (C_2H_4) at a wide range of experimental impact energies from 400 to 2400 eV confirmed that the observed "turn up" effects of $(e,2e)$ cross sections in the low-p region of the π^*-like molecular orbital are due to the distorted wave effects [34]. In addition, as the third possible reason, the modest quality of the exchange correlation functionals and basis sets that we have employed in our calculations might also lead to the discrepancies between theory and experiment.

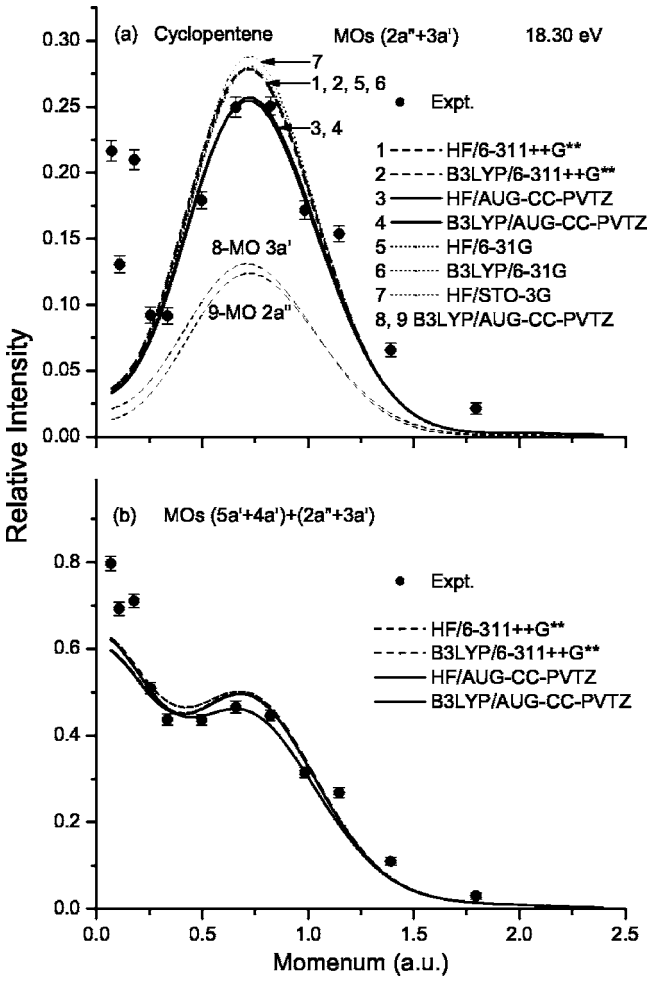

FIG. 6. Experimental and theoretical momentum distributions for (a) the $2a''$ and $3a'$ orbitals and (b) the summed $(5a'+4a')$ and $(2a''+3a')$ orbitals of cyclopentene. The solid circles represent the experimental measurements derived from deconvolution procedures. The theoretical momentum profiles are calculated by using HF and DFT-B3LYP methods with various basis sets.

Experimental and theoretical momentum profiles for the summed $5a'$ and $4a'$ orbitals are shown in Fig. 5. Both the experimental and theoretical momentum profiles display a mainly "*s*-type" distribution with a secondary maximum. It can be seen from the DFT-B3LYP calculations that the $5a'$ orbital has a "*p*-type" distribution (curve 8) while the $4a'$ orbital has an "*s*-type" distribution with a secondary maximum at ~0.8 a.u. (curve 9). As for the summed $5a'$ and $4a'$ orbitals, the DFT-B3LYP and HF calculations with the polarized and diffuse basis sets (curves 1–4) can provide good description of the experimental data. Under comparison within these calculations, the DFT calculation with the AUG-CC-PVTZ basis set (curve 4) can provide a somewhat better fit to the experimental data. The DFT and HF calculations with the lower-level 6-31G basis set (curves 5 and 6) are similar and have the relatively low intensity in the lower momentum region for the experimental data. The HF result with the minimal STO-3G basis set shows a much lower intensity in the lower momentum region (curve 7).

The momentum distributions of the $2a''$ and $3a'$ orbitals have "*p*-type" character as indicated by the DFT-B3LYP calculations with the AUG-CC-PVTZ basis set (curves 8 and 9) in Fig. 6(a). The comparison between experimental data and theoretical calculations in Fig. 6(a) indicates that the HF and DFT calculations with the AUG-CC-PVTZ basis set (curves 3 and 4) give the proper intensity in the above 0.2 a.u. momentum region and the correct position of the maximum. All other calculations (curves 1, 2 and 5–7) overestimate the observed intensity in this momentum region. However, there is a significant discrepancy between theoretical calculation and experimental data in the lower momentum region (below

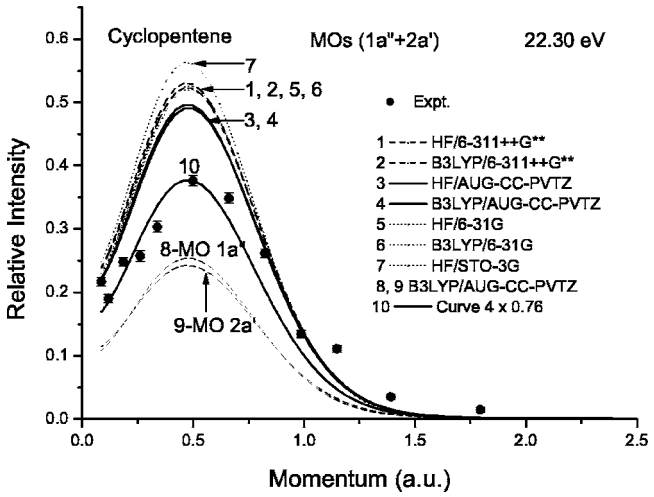

FIG. 7. Experimental $(1a''+2a')$ and theoretical momentum distributions for the $1a'',2a'$ orbital and the sum of the individual orbitals of cyclopentene. The solid circles represent the experimental measurements derived from deconvolution procedures. The theoretical momentum profiles are calculated by using HF and DFT-B3LYP methods with various basis sets. The curve 10 is due to the curve 4 multiplied by an estimated pole strength of 0.76.

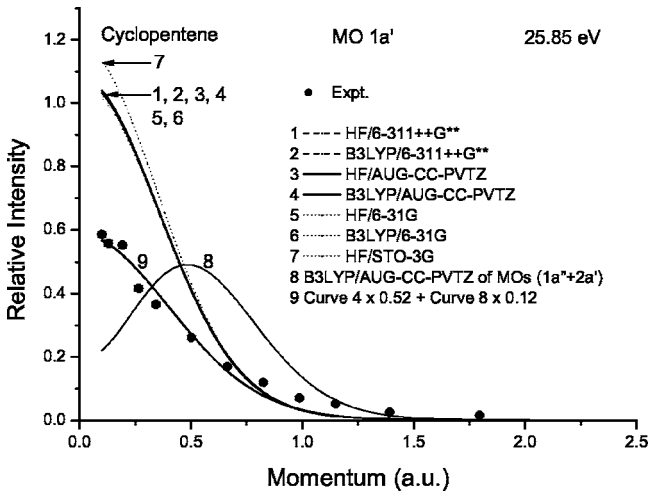

FIG. 8. Experimental and theoretical momentum distributions for the innermost valence orbital $1a'$ of cyclopentene. The solid circles represent the experimental measurements derived from deconvolution procedures. The theoretical momentum profiles are calculated by using HF and DFT-B3LYP methods with various basis sets. The curve 9 represents a sum of $0.52\times$curve 4 plus $0.12\times$curve 8.

0.2 a.u.) and the TMPs underestimate the experimental intensity. The discrepancy between experiment and theory in the low momentum region is probably due to uncertainty in the curve-fitting procedures. In order to further investigate the "turn up" effect of $2a''$ and $3a'$ orbitals in the low momentum region, the summed experimental data of the $(5a'+4a')$ and $(2a''+3a')$ orbitals are compared with the summed theoretical calculations in Fig. 6(b). Then the summed TMPs give a very reasonable description for the summed XMP above 0.2 a.u., and underestimate the experimental data in the low momentum region. Upon further considering the better agreements between experiment and theory of $5a'$ and $4a'$ orbitals electron momentum profiles, we could conclude that the discrepancy between experimental data and theoretical calculations below 0.2 a.u. for the $2a''$ and $3a'$ orbital is not mainly due to a possible uncertainty in the curve-fitting procedures. The other possible reasons for this discrepancy could be the modest quality of our theoretical calculations and the distorted wave effects since the $2a''$ and $3a'$ orbitals of cyclopentene have the π^*-like characters [32–35].

The inner valence band located at 22.30 eV of the binding-energy spectrum in Fig. 1 includes the $1a''$ and $2a'$ orbitals. It can be seen from the experimental data and the theoretical calculations that the summed momentum profiles of the two orbitals have the "*p*-type" distributions shown in Fig. 7. The theoretical calculations indicate that the $1a''$ and $2a'$ orbitals have a "*p*-type" distribution (curves 8 and 9). The comparison between the experimental data and the summed theoretical calculations in Fig. 7 shows that all seven calculations significantly overestimate the experimental intensity (curves 1–7). This indicates that some of the transition intensity from this orbital is located in the higher-binding-energy range due to the final-state electron-correlation effects. In order to compare the momentum distribution, the DFT-B3LYP calculation with AUG-CC-PVTZ is multiplied by an estimated pole strength of 0.76 and the reproduced momentum profile is represented by curve 10 in Fig. 7. A good shape agreement between experiment and theory is then achieved.

The last peak, located at 25.85 eV in the inner valence region of the EMS binding-energy spectrum in Fig. 1, is mainly due to the ionization of the $1a'$ orbital which has an "*s*-type" symmetry, as shown in Fig. 8. The calculated momentum distributions for the $1a'$ orbital are compared with the experimental data in Fig. 8. It is obvious that all seven calculations (curves 1–7) overestimate the experimental intensity. A strong splitting for the $1a'$ orbital into the higher binding-energy region is observed (see Fig. 1) due to the final-state electron-correlation effects. From the above-mentioned discussion about the $1a''$ and $2a'$ orbitals, it should also be noted that this energy range around 24 eV may include some intensity from the $1a''$ and $2a'$ orbitals. Therefore, estimated spectroscopic factors of 0.52 and 0.12 are used to multiply the DFT-B3LYP calculation with the AUG-CC-PVTZ basis set for the $1a'$ and the summed $1a''$ and $2a'$ orbitals, respectively, and the summed theoretical curve, represented by curve 9 in Fig. 8, is then compared with the XMP. With the above shape matching scaling factors, a good fit to experimental data is obtained.

V. SUMMARY

In summary, the measurements of the complete valence shell electron density distributions and binding-energy spectrum for cyclic unsaturated cyclopentene by a binary $(e,2e)$ electron momentum spectrometer are reported. The experimental momentum distributions are compared with the extensive calculations using both HF and DFT methods.

On the basis of the comparisons between the experimental and theoretical valence shell electron density distributions, the most physically reasonable representation of the cyclopentene wave functions can be provided by the calculations with the AUG-CC-PVTZ basis set, which indicates that the basis set including saturated diffuse and Dunning's correlation consistent polarization is essential for the cyclic unsaturated hydrocarbon molecules. The DFT calculations using the B3LYP hybrid functional with the saturated diffuse and Dunning's correlation consistent polarization basis set can provide a relatively good description of the measured momentum profiles, especially the HOMO and the summed $5a'$ and $4a'$ orbitals. Some significant discrepancies between experiment data and theoretical calculations were observed in the $3a''$, $2a''$, and $3a'$ orbitals, which are mainly due to possible distorted wave effects and theoretical calculation qualities.

The inner valence orbital ionizations ($2a'$, $1a''$, and $1a'$ orbitals) are consistent with the pole strengths for ionization from these orbitals being split into higher-energy satellite processes, which is due to many-body ion states associated with the inner valence orbital ionization.

ACKNOWLEDGMENTS

This project was supported by the National Natural Science Foundation of China under Grants No. 19854002, No. 19774037, and No. 10274040 and the Research Fund for the Doctoral Program of Higher Education under Grant No. 199900032.

[1] J. H. Cho and L. Kleinman, Phys. Rev. B **64**, 235420 (2001).
[2] Y. Yamashita, K. Hamaguchi, S. Machida, K. Mukai, J. Yoshinobu, S. Tanaka, and M. Kamada, Appl. Surf. Sci. **169–170**, 172 (2001).
[3] G. P. Lopinski, D. D. M. Wayner, and R. A. Wolkow, Nature (London) **406**, 48 (2000).
[4] J. S. Hovis, H. Liu, and R. J. Hamers, Surf. Sci. **402–404**, 1 (1998).
[5] H. B. Liu and R. J. Hamers, Surf. Sci. **416**, 354 (1998).
[6] H. B. Liu and R. J. Hamers, J. Am. Chem. Soc. **119**, 7593 (1997).
[7] R. J. Hamers, J. S. Hovis, S. Lee, H. B. Liu, and J. Shan, J.

Phys. Chem. B **101**, 1489 (1997).
[8] S. W. Lee, J. S. Hovis, S. K. Coulter, R. J. Hamers, and C. M. Greenlief, Surf. Sci. **462**, 6 (2000).
[9] J. H. Cho and L. Kleinman, Phys. Rev. B **65**, 245407 (2002).
[10] C. E. Brion, G. Cooper, Y. Zheng, I. V. Litvinyuk, and I. E. McCarthy, Chem. Phys. **270**, 13 (2001).
[11] K. Fukui, Angew. Chem., Int. Ed. Engl. **21**, 801 (1982).
[12] M. K. Leong, V. S. Mastryukov, and J. E. Boggs, J. Mol. Struct. **445**, 149 (1998).
[13] S. Saebp, F. R. Cordell, and J. E. Boggs, J. Mol. Struct.: THEOCHEM **104**, 221 (1983).
[14] I. E. McCarthy and E. Weigold, Rep. Prog. Phys. **54**, 789 (1991).
[15] C. E. Brion, Int. J. Quantum Chem. **29**, 1397 (1986).
[16] E. Weigold and I. E. McCarthy, *Electron Momentum Spectroscopy* (Kulwer Academic/Plenum Publishers, New York, 1999).
[17] D. L. Cooper and N. L. Allan, J. Am. Chem. Soc. **114**, 4773 (1992).
[18] S. Knippenberg, K. L. Nixon, M. J. Brunger, T. Maddern, L. Campbell, N. Trout, F. Wang, W. R. Newell, M. S. Deleuze, J. P. Francois, and D. A. Winkler, J. Chem. Phys. **121**, 10525 (2004).
[19] P. Duffy, D. P. Chong, M. E. Casida, and D. R. Salahub, Phys. Rev. A **50**, 4707 (1994).
[20] J. K. Deng, G. Q. Li, Y. He, J. D. Huang, X. D. Wang, F. Wang, Y. A. Zhang, C. G. Ning, N. F. Gao, Y. Wang, X. J. Chen, and Y. Zheng, J. Chem. Phys. **114**, 882 (2001).
[21] W. J. Hehre, R. F. Stewart, and J. A. Pople, J. Chem. Phys. **51**, 2657 (1969).
[22] W. J. Hehre, R. Ditchfield, R. F. Stewart, and J. A. Pople, J. Chem. Phys. **52**, 2769 (1970).
[23] W. J. Hehre, R. Ditchfield, and J. A. Pople, J. Chem. Phys. **56**, 2257 (1972).
[24] R. Krishnan, J. S. Binkley, R. Seeger, and J. A. Pople, J. Chem. Phys. **72**, 650 (1980).
[25] T. Clark, J. Chandrasekhar, and P. v. R. Schleyer, J. Comput. Chem. **4**, 294 (1983).
[26] T. H. Dunning, Jr., J. Chem. Phys. **90**, 1007 (1989).
[27] D. E. Woon and T. H. Dunning, Jr., J. Chem. Phys. **98**, 1358 (1993).
[28] P. Duffy, M. E. Casida, C. E. Brion, and D. P. Chong, Chem. Phys. **159**, 347 (1992).
[29] K. Kimura, S. Katsumata, Y. Achiba, T. Yamazaki, and S. Iwata, *Handbook of HeI Photoelectron Spectra of Fundamental Organic Molecules* (Japan Scientific Society, Tokyo, 1981).
[30] K. B. Wiberg, G. B. Ellison, J. J. Wendoloski, C. R. Brundle, and N. A. Kuebler, J. Am. Chem. Soc. **98**, 7179 (1976).
[31] D. G. Streets and A. W. Potts, J. Chem. Soc., Faraday Trans. 2 **70**, 1505 (1974).
[32] M. J. Brunger, S. W. Braidwood, I. E. McCarthy, and E. Weigold, J. Phys. B **27**, L597 (1994).
[33] C. E. Brion, Y. Zheng, J. Rolke, J. J. Neville, I. E. McCarthy, and J. Wang, J. Phys. B **31**, L223 (1998).
[34] X. G. Ren, C. G. Ning, J. K. Deng, S. F. Zhang, G. L. Su, F. Huang, and G. Q. Li, Phys. Rev. Lett. **94**, 163201 (2005).
[35] J. K. Deng, G. Q. Li, X. D. Wang, J. D. Huang, H. Deng, C. G. Ning, Y. Wang, and Y. Zheng, J. Chem. Phys. **117**, 4839 (2002).